

MOLECULAR GAS AND STAR FORMATION IN BARS OF NEARBY SPIRAL GALAXIES

KARTIK SHETH¹

Division of Mathematical and Physical Sciences, California Institute of Technology, Pasadena, CA 91125; and Department of Astronomy, University of Maryland, College Park, MD 20742-2421; kartik@astro.caltech.edu

STUART N. VOGEL

Department of Astronomy, University of Maryland, College Park, MD 20742-2421; vogel@astro.umd.edu

MICHAEL W. REGAN¹

Space Telescope Science Institute, Baltimore, 3700 San Martin Drive, MD 21218; mregan@stsci.edu

PETER J. TEUBEN AND ANDREW I. HARRIS

Department of Astronomy, University of Maryland, College Park, MD 20742-2421;
 teuben@astro.umd.edu, harris@astro.umd.edu

AND

MICHELE D. THORNLEY¹

Department of Physics, Bucknell University, Lewisburg, PA 17837; mthornle@bucknell.edu

Received 2002 May 16; accepted 2002 July 31

ABSTRACT

We compare the distribution of molecular gas and star formation activity in the bar region of six spirals (NGC 2903, 3627, 4321, 5457, 6946, and IC 342) from the BIMA Survey of Nearby Galaxies. The molecular gas, traced using the CO ($J = 1-0$) emission line, is brightest along the leading edge of the stellar bar in the bar dust lanes. The star formation activity, traced using the H α emission line, is offset toward the leading side of the CO emission. A cross-correlation analysis shows that (1) the H II regions are offset 0–800 pc on the leading side of the CO emission, (2) the largest offsets are found in the strongest bars, and (3) there is a wide range in offsets in a single bar with no systematic pattern as a function of the galactocentric radius. The CO-H α offset constrains how stars may form depending on the gas flow. We examine possible star formation scenarios in context of the two main classes of bar gas-flow simulations, the N -body/sticky particle and hydrodynamic models. Though both model gas flows are generally consistent with the observed offsets, we suggest the inclusion of a two-phase or multiphase medium to improve the agreement between models and observations.

Key words: galaxies: evolution — galaxies: ISM — galaxies: kinematics and dynamics — galaxies: spiral — ISM: molecules — stars: formation

1. INTRODUCTION

Barred spiral galaxies are ideal laboratories for the study of star formation because they host a variety of environments with distinctive star formation activity and gas dynamics. These environments include the circumnuclear, inner and outer rings (see discussion of rings in Buta & Combes 1996; Regan et al. 2002), the bar ends, and the bar region itself, located in between the bar ends and the nucleus. From region to region the star formation activity can vary dramatically: bars have star formation rates of $\sim 0.1\text{--}0.4 M_{\odot} \text{ yr}^{-1}$ (e.g., Martin & Friedli 1997), whereas in circumnuclear rings, in an area 10–30 times smaller, star formation rates may be as high as $1 M_{\odot} \text{ yr}^{-1}$ (e.g., Buta et al. 2000). Since star formation occurs in molecular clouds, comparative studies of the distribution of molecular gas and star formation activity in different environments can shed light on how star formation may be induced or inhibited.

Along the spiral arms, for example, observations find that the molecular gas and H II regions are usually not cospatial; H II regions are preferentially offset toward the leading side

of the molecular gas or dust lanes (Vogel, Kulkarni, & Scoville 1988; Rand 1993; Knapen & Beckman 1996; Loinard et al. 1996). This offset is interpreted as evidence of star formation induced by a spiral density wave (Vogel, Kulkarni, & Scoville 1988; Rand 1993). However, such offsets are not universally present. In M100 Sempere & Garcia-Burillo (1997) find that the offset is absent, or even inverted, along the spiral arms. Still, in other cases, the offset is more pronounced between the H II regions and the dust lanes as the molecular gas and dust lanes diverge (e.g., Lord & Kenney 1991; Rand, Lord, & Higdon 1999). Rand et al. (1999) attribute the divergence to heating of the gas by young stars or cosmic rays, or to a two-phased molecular gas medium, but admit that neither of these explanations works satisfactorily.

In barred spirals most previous studies comparing the molecular gas distribution and star formation activity have focused on the highly active circumnuclear region (e.g., Eckart et al. 1991; Roy & Belley 1993; Kenney, Carlstrom, & Young 1993; Sakamoto et al. 1995; Benedict, Smith, & Kenney 1996). In this paper we focus on the unique region between the bar ends and the nucleus. This region is unlike any other in the galactic disk because it is dominated by highly elliptical stellar orbits (see reviews by Sellwood & Wilkinson 1993; Athanassoula 1992a, 1992b). Throughout this paper, we refer to it simply as the *bar*.

¹ Visiting Astronomer, Kitt Peak National Observatory, National Optical Astronomy Observatory, which is operated by the Association of Universities for Research in Astronomy, Inc., under cooperative agreement with the National Science Foundation.

Only one previous study has studied the location of H II regions relative to the stellar bar (Martin & Friedli 1997); they found that the “H α bar” was usually offset toward the leading side of the stellar bar, with misalignments as large as 15°. Studies of molecular gas or dust in bars have found that the gas and dust are also on the leading side of the stellar bar (e.g., Ondrechen 1985; Handa et al. 1990; Regan & Vogel 1995; Downes et al. 1996; Sheth et al. 2000). But the relationship between the molecular gas (or dust) and star formation has only been studied in a few cases. In M101, for example, Kenney, Scoville, & Wilson (1991) note that the molecular gas and H α emission are at the same position angle. In contrast, Sheth et al. (2000) found that the H II regions in the bar of NGC 5383 are offset toward the leading side of the bar dust lanes. It is unclear whether such offsets are common in bars. Since bars have distinctive (and well-studied) gas kinematics, a study of the relative distribution of the gas and stars can further elucidate the complex phenomenon of star formation. With this goal, we have studied six barred spirals from the recently completed BIMA Survey of Nearby Galaxies (SONG) (Regan et al. 2001; Helfer et al. 2002b).

The sample selection is discussed in § 1.1, and the observations and data reduction in § 2. Using the CO ($J = 1-0$) emission line to trace the molecular gas and the ionized hydrogen (H α) line to trace recent star formation activity, we compare the relative distribution of the two in § 3.1. In all six galaxies we find that the majority of the H α emission is offset toward the leading side of the molecular gas.

We quantify the offset using one- and two-dimensional cross-correlation analysis in § 3.2. The CO-H α offset constrains how stars may form, depending on the gas flow into the dust lane. We discuss the results of the cross-correlation analysis in the framework of the two main classes of bar gas-flow models (the N -body sticky particle and hydrodynamic models) in § 4 and summarize our results in § 5.

1.1. Sample Selection

In BIMA SONG (see details of the survey in Regan et al. 2001; Helfer et al. 2002b), we detect CO emission in 27 of

the 29 barred spirals (e.g., Figs. A1 and A2 in Sheth 2001²). Typically, the emission is detected in the circumnuclear region, where it is usually the brightest. In some bars CO emission is also detected at the bar ends, along the bar, and even in inner rings (Regan et al. 2002). Since we are mainly interested in studying star formation in the bar region, we limit ourselves to those BIMA SONG galaxies in which *both* CO and H α emission are clearly detected over a significant portion of the bar. Six galaxies satisfy this criterion: NGC 2903, 3627, 4321, 5457, 6946, and IC 342. Global properties of these six are listed in Table 1.

Though small, our sample spans a range of Hubble types with 1 Sb, 2 Sbc, and 3 Scd galaxies. This range may be important because most of the observed differences in star formation activity in bars occur between early and late Hubble-type galaxies (e.g., Elmegreen & Elmegreen 1985; Ohta, Sasaki, & Saito 1986). For instance, early Hubble-type bars have low star formation activity along the bar and high star formation activity at the bar ends, whereas late Hubble-type galaxies have higher star formation activity in the bar but have a gap in star formation at the bar ends (Phillips 1996).

All the galaxies in our sample are classified as SAB in the RC3 catalog. However, this does not mean that they are all weak bars because the Hubble classification of SAB types is not rigorous; in fact, a recent analysis of infrared data has shown that the true fraction of strong bars may be as high as 56%, higher than the typically quoted 33% in the RC3 (Eskridge et al. 2000). The strength of a bar may be correlated with its Hubble type. Elmegreen & Elmegreen (1985) concluded that early Hubble-type galaxies have stronger bars because these bars are longer relative to their disks and have flat profiles; these galaxies also have strong spiral arm patterns. However, bar strength is a difficult parameter to quantify; other structural properties, such as the bar ellipticity and bulge size, are also important (see discussion in Buta & Block 2001).

² At <http://www.astro.caltech.edu/~kartik/thesis.html>.

TABLE 1
PROPERTIES OF OBSERVED GALAXIES

Galaxy	Type RC3	R.A. ^a (J2000.0)	Decl. (J2000.0)	V_{hel} (km s ⁻¹)	P.A. (deg)	i (deg)	D (Mpc)
IC 342	SAB(rs)cd	03 46 48.56	+68 05 46.6	34	37	31.00	2.10 ¹
NGC 2903	SAB(rs)bc	09 32 10.05	+21 30 02.0	556	17	61.40	7.30 ²
NGC 3627	SAB(s)b	11 20 14.99	+12 59 29.3	727	173	62.80	11.07 ³
NGC 4321	SAB(s)bc	12 22 54.84	+15 49 20.0	1571	30	31.7	16.1 ⁴
NGC 5457	SAB(rs)cd	14 03 12.52	+54 20 56.5	241	35	21.05	6.45 ⁵
NGC 6946	SAB(rs)cd	20 34 52.33	+60 09 14.2	48	35	31.66	6.40 ⁶

NOTE.—Units of right ascension are hours, minutes, and seconds, and units of declination are degrees, arcminutes, and arcseconds.

^a Galaxy centers measured from either our optical data or from the 2MASS survey. Position angle (P.A.), inclination (i), Hubble type, and the heliocentric velocity (V_{hel}) are from the RC3 catalog. References for the adopted distances (D) are given below.

¹ Karachentsev & Tikhonov 1993.

² Planesas, Colina, & Perez-Olea 1997.

³ Saha et al. 1999.

⁴ Ferrarese et al. 1996.

⁵ Stetson et al. 1998.

⁶ Sharina, Karachentsev, & Tikhonov 1997.

A good indicator of the bar strength is the shape of the bar dust lanes because it reflects the gas response to the stellar bar. Athanassoula (1992b) showed that strong bars have relatively straight dust lanes, whereas weaker bars have curved dust lanes. Extending her analysis to our sample, we infer that NGC 2903 and NGC 3627 are strongly barred because of their straight dust lanes. NGC 5457 and NGC 4321, with slightly curved dust lanes, are weaker bars. IC 342 has even more curved dust lanes, indicating an even weaker bar. In NGC 6946 the northern dust lane appears to be straight, but the southern dust lane is curved, so it is difficult to classify this bar solely on the shape of the dust lanes. Regan & Vogel (1995) suggest that, if there is bar in NGC 6946, it is rather weak. Using bar dust lanes as a measure of bar strength, we find that the three latest Hubble types in our sample are classified as relatively weak bars. In summary, our sample contains a broad range of bar strengths, from strong bars in NGC 2903 and NGC 3627 to intermediate-strength bars in NGC 4321 and NGC 5457 to relatively weak bars in NGC 6946 and IC 342.

2. OBSERVATIONS AND DATA REDUCTION

2.1. Molecular Gas Data

All six galaxies were observed in the CO ($J = 1-0$) emission line with the BIMA (Berkeley-Illinois-Maryland Association) array and the NRAO³ 12 m single-dish telescope as part of the BIMA SONG key project. The 44 galaxy SONG sample was chosen with the following criteria: heliocentric velocity, $V_{\text{HEL}} < 2000 \text{ km s}^{-1}$, declination, $\delta > -20^\circ$, inclination, $i < 70^\circ$, and apparent magnitude, $B_T < 11$. The typical data cube has a synthesized beam of $6''$ and a field of view of $3'$. In a 10 km s^{-1} channel the typical noise is $\sim 58 \text{ mJy beam}^{-1}$. Further details of the data acquisition and reduction can be found in Regan et al. (2001) and Helfer et al. (2002b).

2.2. H α Data

We observed NGC 2903, 3627, and 4321 at the 0.9 m telescope at Kitt Peak on the nights of 1999 April 4–6, with the T2KA 2048×2048 CCD camera in $f/13.5$ direct-imaging mode. In this mode the camera has a $13.1'$ field of view with 0.384 pixels. In the broadband R filter we took three exposures of 180 s each, and in the H α filter ($\lambda_0 = 6573 \text{ \AA}$, $\Delta\lambda = 67 \text{ \AA}$) we took three exposures of 100–140 s each. We divided each frame by a normalized flat-field frame and combined the resulting frames into one single image for each corresponding filter. Then, from these images, we subtracted the mean sky brightness and removed cosmic rays, using standard routines in the NOAO/IRAF⁴ software package. We also corrected all images for atmospheric extinction. Finally, we registered foreground stars in each image with the Hubble Guide Star Catalog (GSC) and determined astrometric solutions for each image. The residuals in determining absolute positions were smaller than $0.2''$; however, systematic errors in the GSC prevent us from achieving an accuracy of less than $1''$. We used the R -band

image to subtract the underlying continuum from the H α image.

We observed IC 342 at the 60 inch (1.5 m) telescope at Palomar⁵ on the night of 1999 November 19 with the Maryland-Caltech Fabry-Perot camera. These data were reduced and calibrated using the procedure described in Vogel et al. (1995). The H α image for NGC 6946 is also a similar velocity-integrated H α Fabry-Perot map obtained previously at Palomar. A broadband continuum image and a continuum-subtracted H α image for NGC 5457 were supplied to us by R. Kennicutt; these images have $2.6''$ pixels, compared with 0.38 pixels for the other optical images.

3. RESULTS

3.1. Comparing the Distribution of Molecular Gas and Star Formation

We first consider the relative distribution of the molecular gas and star formation activity in the six galaxies by overlaying the CO emission on the continuum-subtracted H α images (Figs. 1–6). Our goal is to learn where the stars may be forming by comparing the relative locations of molecular clouds and H II regions. Since any image is only a snapshot in time, it is difficult to assign a star-forming region to its parent molecular complex. We make the usual assumption, that CO traces regions most prone to star formation and H α traces young stars most likely to have formed in molecular gas complexes traced by the CO.

In every image we show the extent of the stellar bar, as determined by Sheth (2001), with an ellipse. The ellipse corresponds to the outermost bar isophote and was determined from fitting ellipses to optical or near-infrared images, following a method devised by Regan & Elmegreen (1997). The width of a bar is a difficult parameter to measure accurately because contamination by bulge light tends to make the fitted ellipses wider (Sheth 2001). Since the minor-axis length is not relevant for the study presented here, we chose a representative minor axis that is one-quarter that of the major axis for all bars except IC 342, which has a small, oval bar, for which we chose a minor axis that is one-half that of the major axis.

In each image (Figs. 1–6) we show CO contours overlaid on a gray-scale image of the continuum-subtracted H α emission. We describe the distribution of H α and CO using approximate position angles because their morphology is often curved. Compact H α structures are labeled with a prefix H, and CO features are labeled with a prefix C. We also show the direction of rotation of the bar with a curved arrow symbol in the lower right hand corner; the direction is based on the assumption that spiral arms trail in galaxies. All the galaxies in our sample rotate counter-clockwise except for NGC 6946.

In all six galaxies we find that the CO emission is brightest on the leading side of the stellar bar. Overlays of the CO maps on optical-infrared color maps (not shown) confirm that the molecular gas generally coincides with the bar dust lanes (Sheth et al. 1998). In five out of the six galaxies weak spurs of CO emission are seen on the trailing (upstream) side of the dust lanes. At the bar ends bright CO emission is

³ The National Radio Astronomy Observatory is a facility of the NSF operated under cooperative agreement by Associated Universities, Inc.

⁴ IRAF is distributed by the National Optical Astronomy Observatory, which is operated by AURA, under cooperative agreement with the NSF.

⁵ The 60 inch telescope at Palomar Mountain is jointly owned by the California Institute of Technology and the Carnegie Institution of Washington.

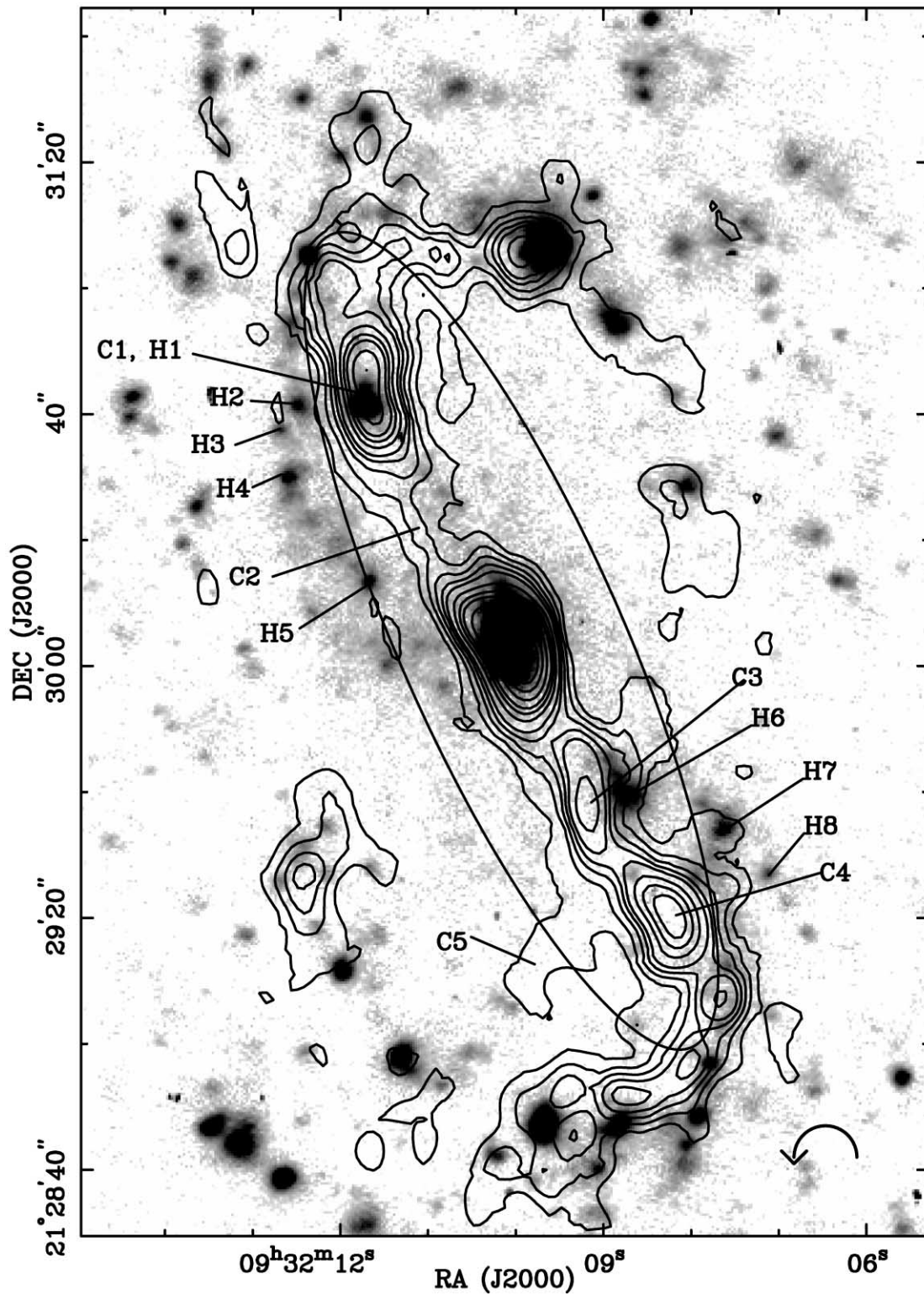


FIG. 1.—NGC 2903: CO(1–0) emission contours from a BIMA SONG + 12 m OTF map overlaid on top of continuum-subtracted $H\alpha$ emission. CO contours are plotted at 2, 4, 6, 8, 10, 14, 18, 22, 30, 40, 50, and $75 \times 2.2 \text{ Jy km s}^{-1}$. The $H\alpha$ image is not calibrated and is shown at an arbitrary stretch. The dark ellipse shows the extent of the stellar bar (Sheth 2001). The curved arrow (*bottom right*) indicates the direction of rotation, assuming that spiral arms trail.

present on the leading and trailing sides; this gas is most likely associated with inner rings, which often encircle bars (Buta & Combes 1996; Regan et al. 2002). The $H\alpha$ emission is distributed in bright, compact structures and weak, diffuse

emission. The differences in bar star formation activity noted by Phillips (1996) are not always present. For instance, both the early Hubble-type bar in NGC 3627 and the late Hubble-type bar in NGC 5457 have relatively little

star formation activity, whereas strong activity can be seen in the bar of NGC 2903. But such differences across Hubble type are difficult to quantify with this small sample. In these six bars, while there are a few cases where $H\alpha$ is coincident with, or on the trailing side of, CO, *all six* show that majority of the $H\alpha$ emission is offset toward the leading side of the CO emission. We describe these results for each individual galaxy in detail below.

NGC 2903 (Fig. 1): The stellar bar in NGC 2903 is oriented at a position angle (P.A.) of 24° east of north. The molecular gas is distributed toward the leading side of the stellar bar, with a P.A. of $\sim 30^\circ$. The $H\alpha$ emission is offset even farther toward the leading side of the CO emission.

In the northern half of the bar, the CO emission is brightest in a large complex labeled “C1.” A bright $H\alpha$ complex, H1, coincides with part of the C1 complex. South of C1 by $3''$ – $4''$ is a narrow ridge of CO, labeled “C2,” which bridges C1 with the bright circumnuclear gas. Several discrete $H\alpha$ features (H2, H3, H4, and H5) are seen on the leading side of the CO. These structures are connected by a diffuse, concave ridge of $H\alpha$ emission. On the trailing (upstream) side some diffuse $H\alpha$ emission is present, but there is a conspicuous lack of H II regions; this is not an artifact of dust extinction. In the dust lanes the dust extinction is usually insufficient to hide H II regions (e.g., Regan & Vogel 1995). Also, the gas density is expected to be dramatically lower on the trailing side of the dust lane as the gas piles up in the bar dust lane (e.g., see model density distributions in Combes & Gerin 1985; Athanassoula 1992b; Piner, Stone, & Teuben 1995).

In the southern half of the bar, there are two bright CO complexes, C3 and C4. As in the northern half, $H\alpha$ complexes (H6, H7, and H8) are all on the leading side of the CO emission. A diffuse ridge of $H\alpha$ emission extends south of H7, with a P.A. of $\sim 5^\circ$, on the leading edge of the CO emission. In this half of the bar we also see a weak CO spur, labeled “C5,” east of C4 on the trailing side of the dust lane. Diffuse $H\alpha$ emission is present at the trailing edge of C5. In two places, near H7 and north of H6, there is weak CO emission on the leading side of the dust lane.

NGC 3627 (Fig. 2): The bar in NGC 3627 is oriented at a P.A. of 161° . The molecular gas is mostly on the leading side of the stellar bar, with a P.A. of $\sim 164^\circ$, but note that, at the southern end of the bar, the molecular gas morphology turns sharply toward the trailing side of the bar. The $H\alpha$ emission is offset toward the leading side of the CO. The CO intensity decreases from the inner ends of the bar toward the outer ends, i.e., from $C3 \rightarrow C2 \rightarrow C1$ in the northern half, and from $C4 \rightarrow C5 \rightarrow C6$ in the southern half. This behavior is consistent with the predictions of the hydrodynamic models (Sheth et al. 2000).

In the northern half of the bar, there is only one bright, compact $H\alpha$ structure, labeled “H1,” located $30''$ north of the nucleus and 3 – $5''$ east and toward the leading side of the CO ridge connecting C1 and C2. Diffuse $H\alpha$ emission connecting H1 to the bar end is also present on the leading edge of the CO. As in NGC 2903 there is a paucity of $H\alpha$ emission on the trailing side of the CO. Additional CO and $H\alpha$ emission associated with an inner ring (*dashed segments*) circumscribing the bar is also present; this inner ring is discussed in detail in Regan et al. (2002).

In the southern half of the bar all three compact $H\alpha$ structures (H2, H3, and H4) are also on the leading edge of the CO emission, 3 – $4''$ west of the CO ridge connecting C4, C5,

and C6. As in the northern half diffuse $H\alpha$ emission connects H2, H3, and H4; most of this emission is also on the leading edge of the CO.

NGC 4321 (Fig. 3): The bar in NGC 4321 is oriented at a P.A. of 102° . The molecular gas is mostly on the leading side of the stellar bar with P.A. $\sim 90^\circ$; this is more clearly seen in the western half of the bar, where the CO emission runs continuously down the entire half of the bar. In the western half the $H\alpha$ emission is offset another $3''$ – $4''$ toward the leading side, with approximately the same P.A. In the eastern half the $H\alpha$ emission is weak and no clear offset is seen.

In the western half of the bar a relatively narrow lane ($10''$ in width) of CO emission emerges from the bright, central $40'' \times 20''$, oval-shaped distribution of CO emission. This lane extends to the west ($C1 \rightarrow C2 \rightarrow C3$) and then curves inward to the spiral arms from C3 to C4. As in NGC 3627 the CO intensity decreases away from the central region. A spurlike feature, labeled “C5,” is seen $5''$ south of C1 extending almost $10''$ (~ 780 pc) on the trailing side of the bar. These spurs may play an important role in forming stars because they have high gas density but are located in an area with lower shear (Sheth et al. 2000).

The discrete $H\alpha$ structures (H1, H2, and H3) are evenly spaced ($\sim 10''$) and are on the leading edge of the CO emission. A narrow ridge of diffuse $H\alpha$ emission connecting these structures is offset north from the CO by about $4''$. Farther west, toward the bar end, a bright concentration of molecular gas, labeled “C4,” is coincident with the brightest $H\alpha$ emission in this half of the bar, labeled “H4.”

In the eastern half of the bar the two main concentrations of CO, C6, and C7 are on the leading side of the stellar bar. Two H II regions, H5 and H6, are offset $\sim 5''$ west of C7 and C6, respectively. Unlike the western half, there is no clear leading offset of H II regions from the CO emission. At the eastern bar end bright CO and $H\alpha$ emission are present in the regions labeled “C8” and “H7.”

CO and $H\alpha$ emission are distributed on the trailing *and* leading sides at the bar ends ($10''$ north of C4 and $12''$ – $15''$ south of C8 and H7). Such a morphology seems to be common in bars and is most likely associated with inner rings (Buta & Combes 1996) that encircle bars.

NGC 5457 (Fig. 4): The bar in NGC 5457 is oriented at a P.A. of 80° . The molecular gas is primarily on the leading side of the stellar bar with P.A. $\sim 95^\circ$. The $H\alpha$ emission tends to be toward the leading side of the CO emission.

In both halves of the bar the CO intensity decreases outward from the central concentration of gas, to the east toward C1 and to the west toward C6. In the western half of the bar there is one bright CO complex, labeled “C2” in Figure 4. Generally coincident with but offset slightly toward the leading side of C2 is a bright H II region, labeled “H1.” Diffuse $H\alpha$ emission connecting the nuclear region and H1 is seen mostly on the leading side of the CO emission in the region in between C1 and C2. To the south of C2, on the trailing side, there is a $10''$ spurlike CO feature, labeled “C3.”

In the eastern half the CO morphology is very similar to that seen in the western half. C7 is a weak CO peak $\sim 30''$ east of the circumnuclear region. Associated with C7 is weak $H\alpha$ emission, labeled “H3.” Generally the $H\alpha$ emission in this half of the bar is characterized by a continuous ridge extending from the circumnuclear emission to H4 on the leading side of the CO. H4, like H2, is on the leading side of the bar and is probably the beginning of an inner ring.

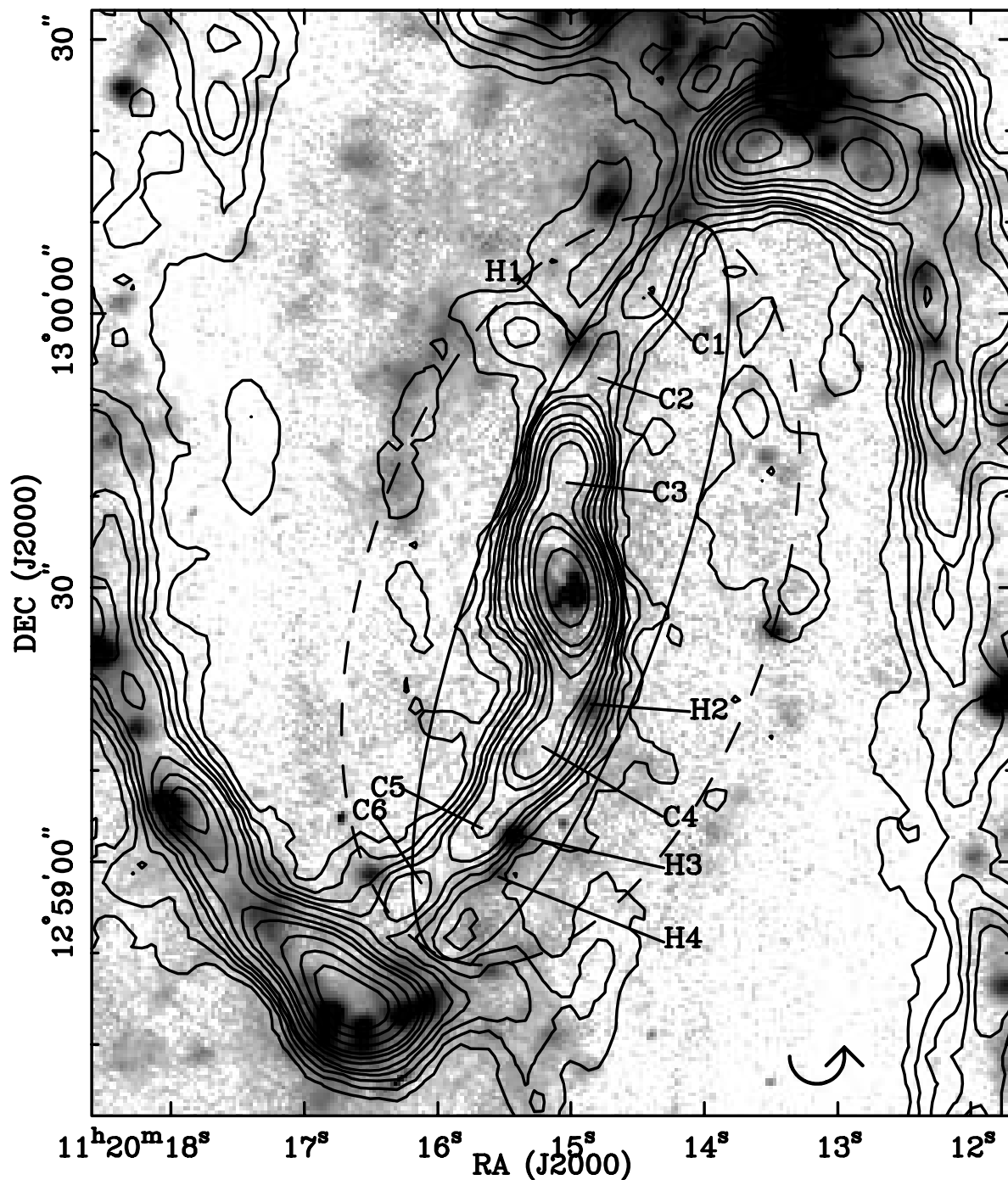


FIG. 2.—NGC 3627: same as Fig. 1. Same CO contour levels as in Fig. 1 $\times 1.4 \text{ Jy km s}^{-1}$. The dashed segments show an inner ring in CO and H α (Regan et al. 2002).

Toward both bar ends the CO emission deviates away from the leading side of the bar and connects with the CO emission in the spiral arms of NGC 5457. The CO region, labeled “C4,” and the H α region, labeled “H2,” are probably associated with the bar end, but the two bright CO and H α peaks 6″–10″ north of H2 are associated with the spiral arm.

NGC 6946 (Fig. 5): The stellar bar in NGC 6946 is oriented at a P.A. of 19°. In the bar the molecular gas is distributed asymmetrically about the center. To the north of the circumnuclear region the CO emission covers a rather

broad 40″ \times 40″ area, with a sharp ridge of CO emission on the leading side of the bar with a P.A. of $\sim 0^\circ$. In the southern half of the bar the broadly distributed CO emission is truncated to the south, extending only 20″ south of the circumnuclear area. While the CO and H α emission overlap considerably, the brightest H α emission tends to be on the leading edge of the CO.

In the northern half of the bar a ridge of CO emission extending from the circumnuclear region toward C1 gradually decreases in intensity. Along this ridge there is an H II region 10″ north of the nucleus, labeled “H1,” a CO peak

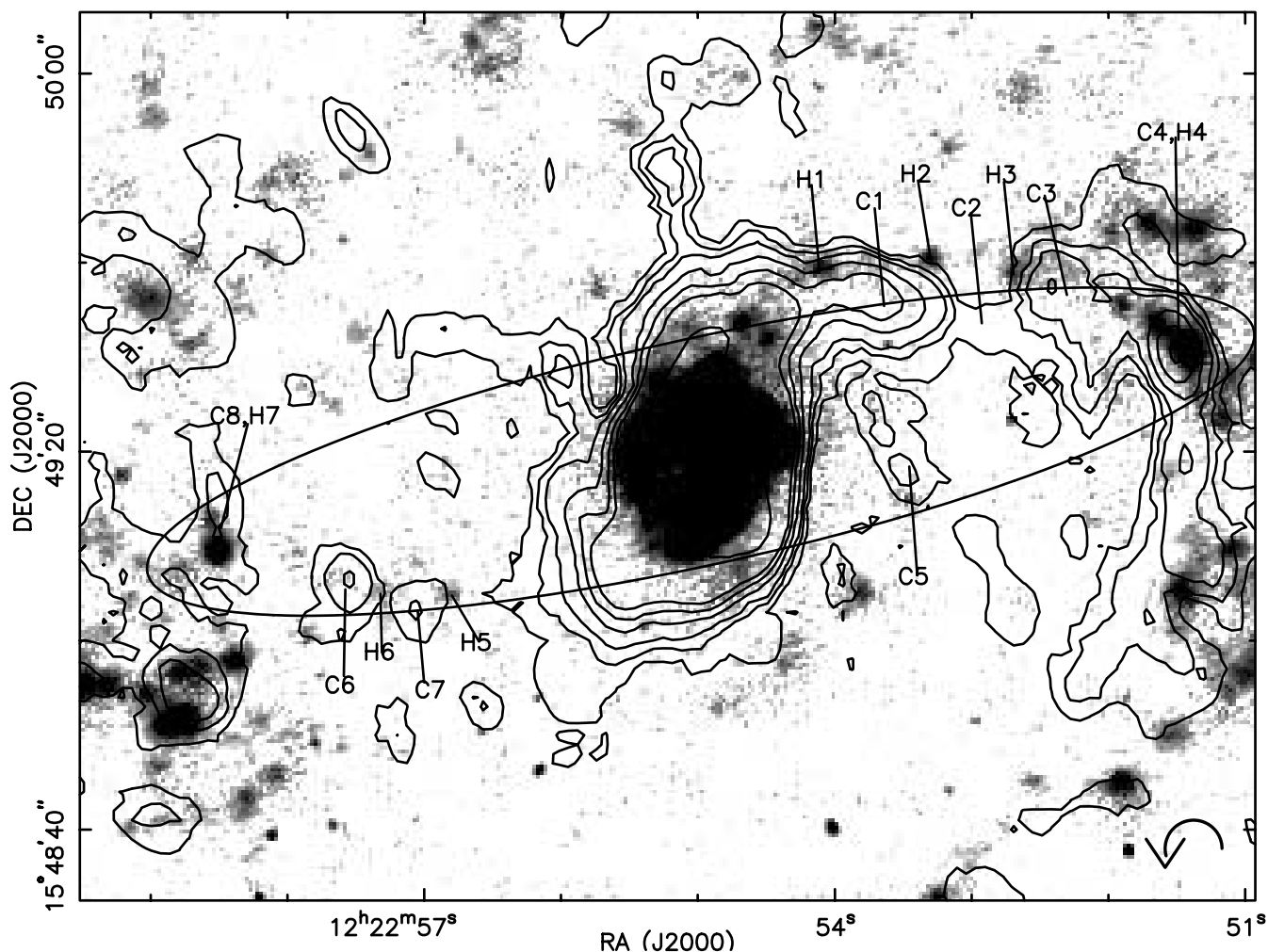


Fig. 3.—NGC 4321: same as Fig. 1. CO contour levels at 2, 3, 4, 6, 8, 10, and $20 \times 2.0 \text{ Jy km s}^{-1}$.

$10''$ farther north, labeled “C1,” and two $\text{H}\alpha$ peaks, labeled “H2” and “H3,” even farther north of C1. We find a significant amount of CO emission on the trailing side of this bar. There is a concentration of CO emission, labeled “C2,” curving east from C1. An H II region is coincident with it. On the trailing side of the bar there is CO emission C3, C4, and C5 and $\text{H}\alpha$ peaks at H4 and H5.

In the southern half a ridge of CO emission extends from the nuclear region toward C7. Associated with C7 is the brightest $\text{H}\alpha$ emission in this half of the bar. Farther south of C7 the CO emission narrows into a ridge, labeled “C9,” and then ends in a broader peak at C10. On the trailing side of C9 is an H II region, labeled “H8.” Two H II regions, H9 and H10, are seen in the leading side of the bar, a few arcseconds northeast of C10. There is also a trailing extension of CO emission to the east of H7, labeled “C8.”

IC 342 (see Fig. 6): IC 342 has a small, oval stellar bar. The bar ellipse shown in Figure 6 is at a P.A. of 28° . The CO emission appears to be in the center of the bar with a P.A. of $\sim 0^\circ$ – 10° . This central distribution of gas is unusual because it is expected only when the bar is extremely strong and inner Lindblad resonances are absent (Athanasoulas 1992b). Such a situation is extremely short-lived in the models. It is more likely that the bar parameters for this galaxy are misidentified because the bar resides in a bright

starburst circumnuclear region. A recent study by (Crosthwaite et al. 2001) suggests that, although the bar is most prominent in the central $2''$, CO kinematics indicate a gaseous bar as long as $4.7'$ with P.A. $\sim 0^\circ$. In that case the CO emission would be on the leading edge of the bar.

As in other bars the CO emission along both dust lanes decreases in intensity outward from the circumnuclear region, toward C2 to the north and C4 to the south. In the northern half of the bar there is an extension of CO, labeled “C1,” toward the trailing side. A few arcseconds north of it is an H II region, labeled “H1,” which also lies along the leading edge of the CO emission. Farther north near the bar end there is a CO emission peak, labeled “C3.” A few arcseconds north and east of C3 is another $\text{H}\alpha$ peak, labeled “H2.”

In the southern half of the bar there is a concentration of CO emission, labeled “C5,” on the trailing side of the main lane of CO emission. There is also a ridge of CO emission that extends southeast of the nucleus toward the bar end, ending in a CO peak, labeled “C6.” In the bar there is a lot of diffuse $\text{H}\alpha$ emission, but the few H II regions (H3 and H4) are on the leading side of the CO ridge.

In summary, CO emission in all six bars is brightest on the leading side of the stellar bar in the bar dust lanes. The CO intensity generally decreases toward the bar ends. Weak

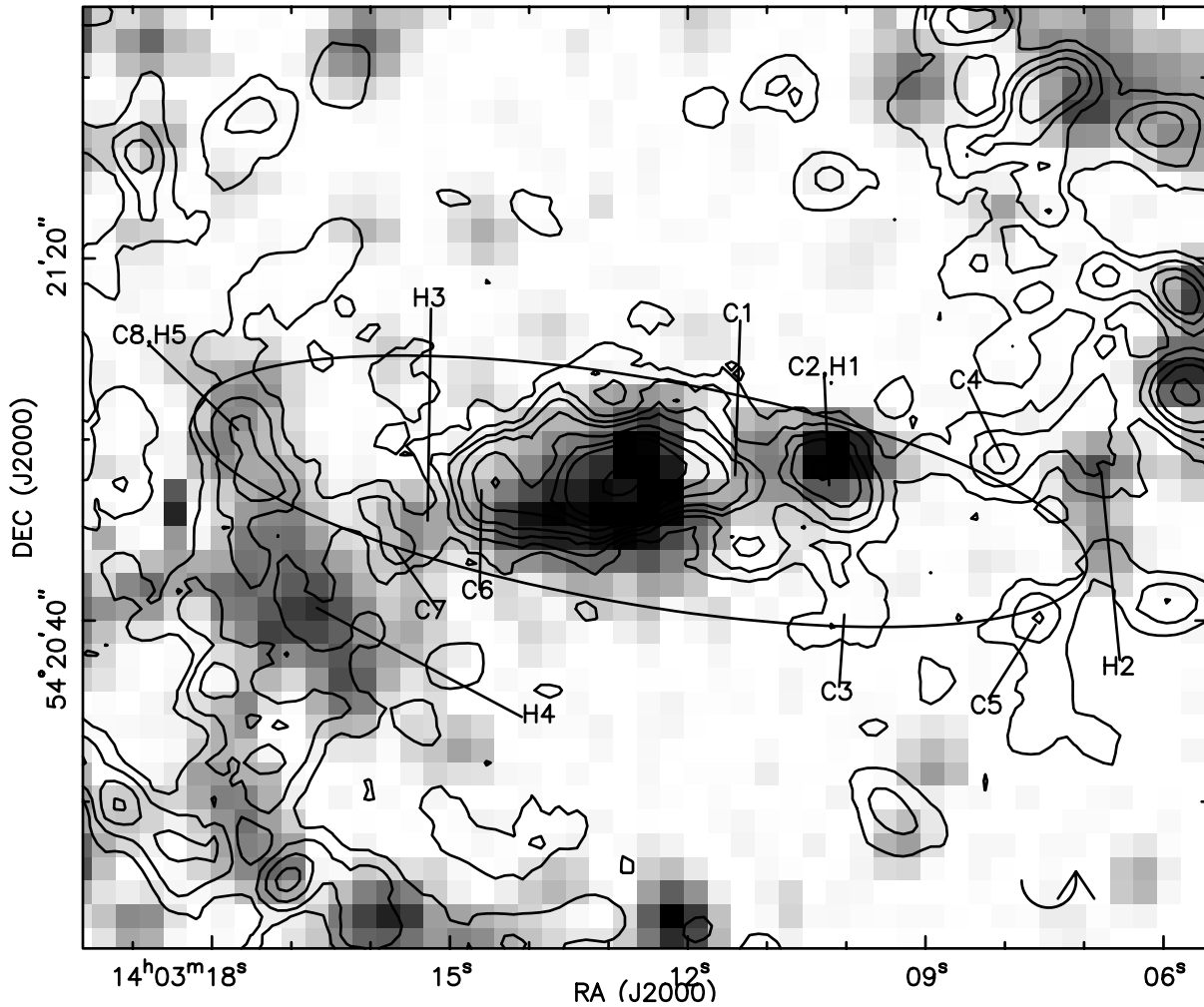


FIG. 4.—NGC 5457: same as Fig. 1. CO contour levels at 1, 2, 3, 4, 6, 8, 10, and $20 \times 1.8 \text{ Jy km s}^{-1}$. The CO and $\text{H}\alpha$ emission in this galaxy have notably different distributions at the bar ends than they do in NGC 2903 or NGC 3627 in that the CO and $\text{H}\alpha$ emission curves toward the leading side of the bar. This gas response is probably related to the properties of this late Hubble-type bar.

spurs of CO emission are sometimes seen on the trailing side of the bar. At the bar ends there is often bright CO and $\text{H}\alpha$ emission on both the trailing and leading sides; this emission is probably associated with inner rings. In a few instances $\text{H}\alpha$ emission is coincident with, or on the trailing side of, the CO emission. But in all six bars the majority of the $\text{H}\alpha$ emission is on the leading side of the molecular gas.

3.2. Quantifying the Offsets

The typical distance between molecular gas complexes and H II regions sheds light on when, where, and how stars form. To accurately measure this distance, we need to trace the orbit of an H II region and measure the separation along this path. In a typical galaxy disk this path is usually circular, and therefore a measurement of the azimuthal displacement is sufficient. However, nonaxisymmetric perturbations, such as bars and spiral arms, can introduce streaming motions in the gas (e.g., Roberts, Huntley, & van Albada 1979; Athanassoula 1992b, and references therein). In these cases an orbit has both an azimuthal and a radial component. The radial displacement depends on the strength of the bar or spiral arm, and it may vary with radius. We expect that the radial streaming motions will be most important at the inner ends of the bar and spiral arms

(Roberts, Huntley, & van Albada 1979). From § 3.1 we infer that, to first order, the displacement is mostly in the azimuthal direction. Therefore, we first quantify the distance between the CO and $\text{H}\alpha$ by doing a one-dimensional cross-correlation in azimuth (as described in the next paragraph), and then we perform a two-dimensional (radial + azimuthal) cross-correlation over the entire bar region.

3.2.1. Cross-Correlation Analysis

We regridded each $\text{H}\alpha$ image to the CO image using standard MIRIAD routines (Sault, Teuben, & Wright 1995), deprojected both images using ZODIAC (Miyashiro 1982; Shopbell 1998) routines developed by ourselves and Gruendl (1996), and then mapped the images on to a polar grid. The deprojected CO (*top left*) and $\text{H}\alpha$ (*bottom left*) images are shown in the left column of Figures 7–12. For the one-dimensional cross-correlation analysis we cross-correlated $1''$ annuli. The results of these analyses are shown in the vertical panel on the right-hand side of Figures 7–12. The star symbols indicate the angular offset corresponding to the maximum of the cross-correlation for that radius. Note that this value averages the offset between the CO and $\text{H}\alpha$ in the two halves of the bar. The solid circles on the deprojected $\text{H}\alpha$ and CO images are the boundaries within

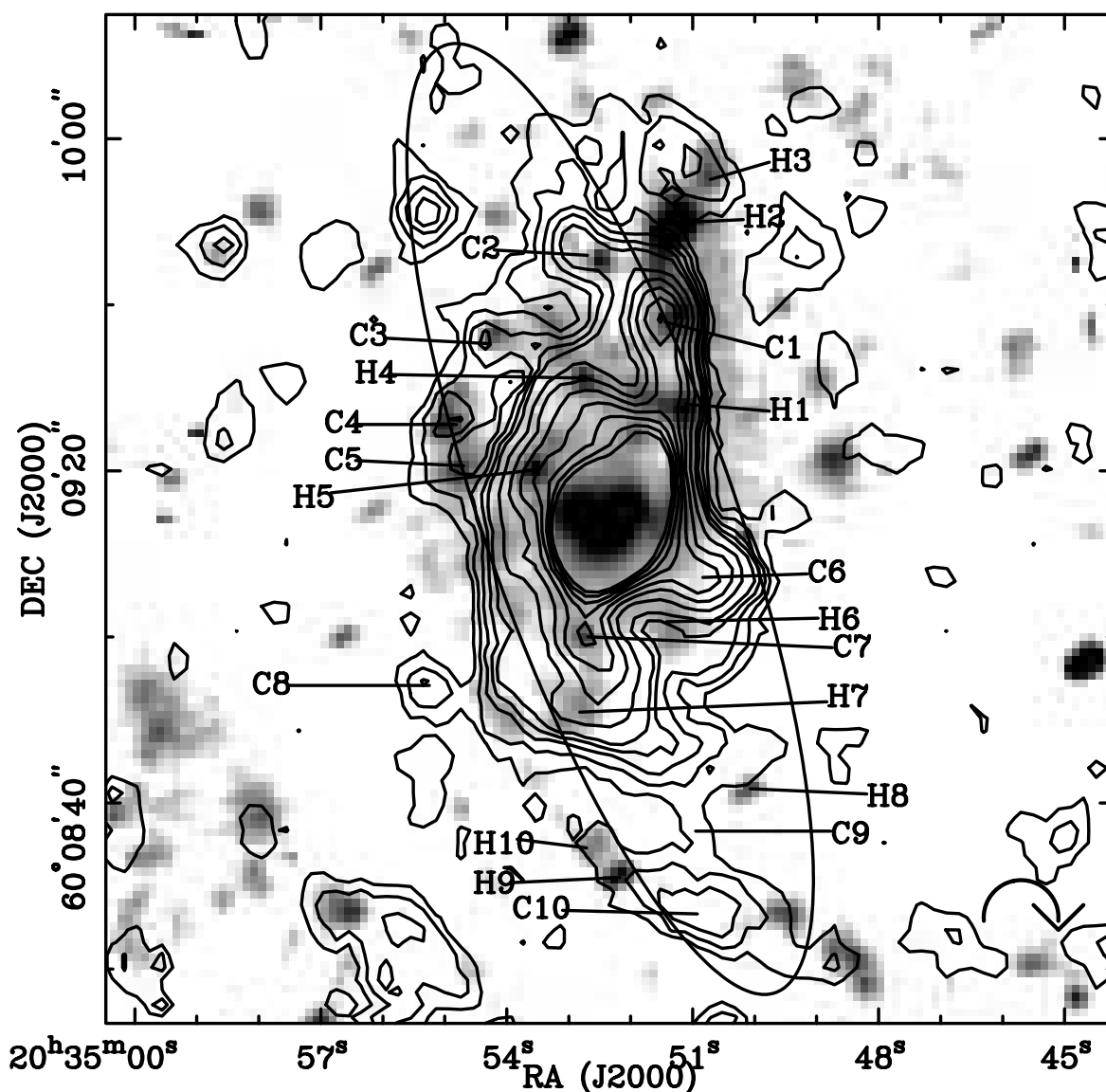


FIG. 5.—NGC 6946: same as Fig. 1. CO contour levels at 2, 4, 6, 8, 10, 15, 20, 25, 30, 35, 40, and $45 \times 2.0 \text{ Jy km s}^{-1}$.

which the cross-correlation is done. The inner radius is chosen to best avoid the circumnuclear emission and the outer radius is at the end of the bar (corresponding to the bar ellipse in Fig. 1–6). The dashed circles are typically spaced at integral multiples of $10''$ and the corresponding radius is shown with a solid, horizontal line in the one-dimensional cross-correlation diagrams in the right-hand panel.

The cross-correlation result can be affected by systematic dust extinction. For example, consider a barred spiral where the $H\alpha$ emission is distributed evenly on the trailing and leading sides. The cross-correlation peak of such a distribution should not show any azimuthal offset. However, if the $H\alpha$ on the trailing side of the dust lane is obscured by a screen of dust, then the cross-correlation diagram would show that the $H\alpha$ is preferentially on the leading side of the dust lane. But, as noted earlier in § 3.1, this is unlikely because the dust extinction on the trailing side is very low as gas piles up in the dust lanes. Note that any extinction suffered by the $H\alpha$ in the dust lane only increases the observed

offsets; so the CO- $H\alpha$ offsets calculated here are upper limits.

It is important to understand whether the cross-correlation peak depends on small, bright structures, like the $H\alpha$ and CO peaks, or on large, diffuse, and dim features. We performed two tests to address this question. First, we flagged all low-level emission in the CO and $H\alpha$ maps of NGC 2903 and cross-correlated the images in radius and azimuth. We found that the cross-correlation peak was essentially unchanged. The main difference was that a background of small but nonzero correlation values, present in the original cross-correlation diagram, was now removed. The diffuse emission, therefore, is analogous to a constant offset contributing to the correlation diagram, but at no particular lag. This test indicates that the cross-correlation peak is determined primarily by the bright peaks in the maps.

As a second test, we set all emission above an arbitrary bright signal value to that signal value in the $H\alpha$ and CO maps for NGC 2903, approximating the removal of bright

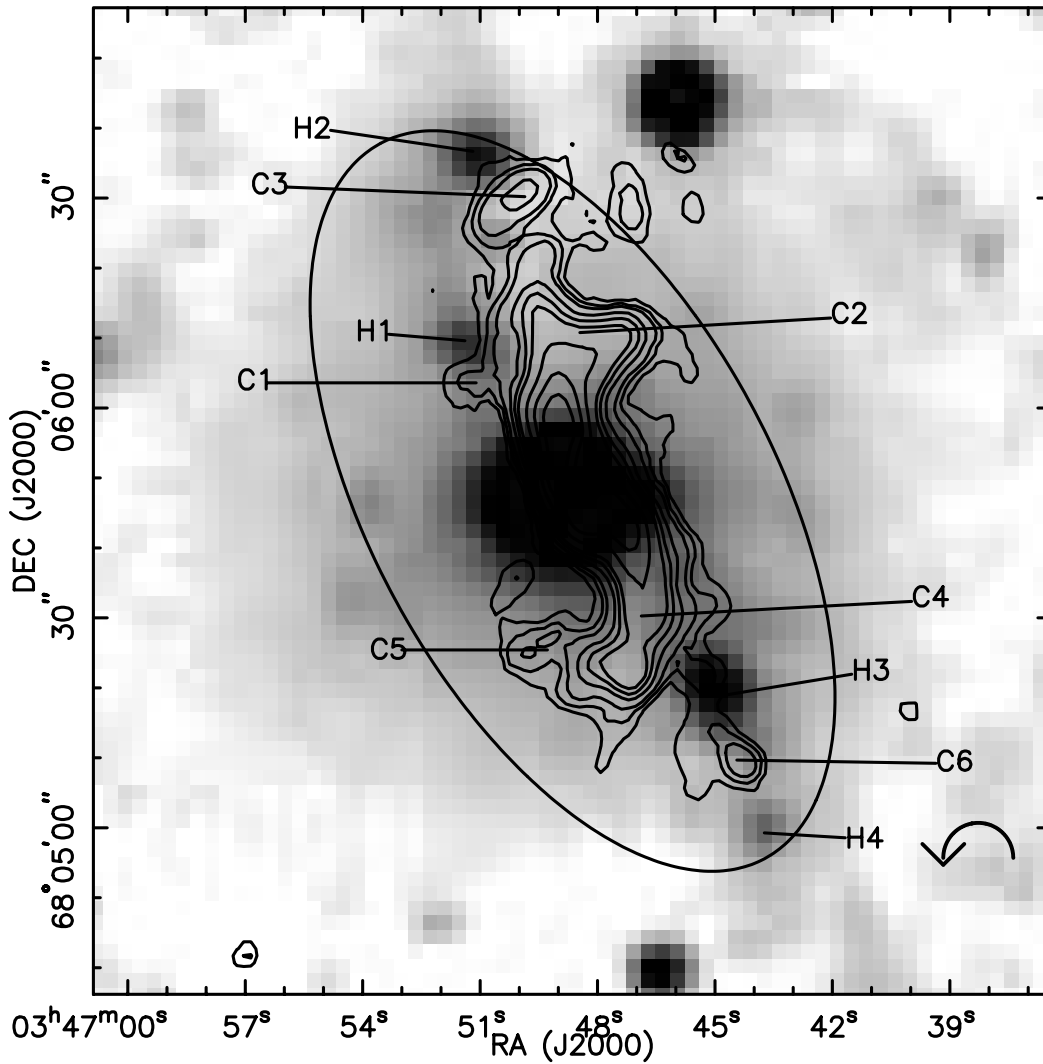


FIG. 6.—IC 342: same as Fig. 1. CO contour levels at 2, 3, 4, 6, 8, 10, 15, 20, 25, 30, 35, 40, $45 \times 5.0 \text{ Jy km s}^{-1}$.

peaks. In the resulting correlation diagram there was a trend of $\text{H}\alpha$ offset azimuthally toward the leading side from the CO, but the cross-correlation peak moved significantly from its original location and became broader. The larger width of the peak was expected because we removed the sharpness inherent in the maps being correlated. The shift, once again, showed that the location of the correlation peak is primarily determined by bright $\text{H}\alpha$ and CO peaks. Assuming that these peaks trace regions most prone to star formation and recently formed OB associations, respectively, the correlation peak effectively quantifies the offset between parent molecular gas complexes and newly formed stars.

3.2.2. Results of the One-dimensional Cross-Correlation

In every bar (*right-hand panels*, Figs. 7–12) we find that the peak of the cross-correlation shows $\text{H}\alpha$ azimuthally offset toward the leading side of the CO emission, consistent with the discussion in § 3.1. In these panels we have annotated the correlation peaks with the notation used in Figures 1–6 for the corresponding CO and HII regions.

The offset between the annotated regions varies from 0–800 pc with a range of offsets in any given bar. We find that

the largest offsets are generally seen in the strongest bars. For instance, in NGC 2903 offsets of ~ 800 pc are seen in the northern half, between C2 and H5, and between H4, H5, and the northern part of C1. In the same bar smaller offsets are also present between C3 and H6 (~ 400 pc) and between C1 and H1 (~ 200 pc). In the slightly weaker bars, NGC 4321 and NGC 5457, the HII regions are typically offset 200–500 pc (e.g., C1 and H1 in Fig. 9), and in the weakest bars, NGC 6946 and IC 342, the offsets are even smaller, typically less than 400 pc.

At some radii the cross-correlation peak is at larger distances, exceeding a kiloparsec in some cases. These are instances where only weak and diffuse $\text{H}\alpha$ emission is being correlated with the CO emission. An example of this is seen between $20''$ – $25''$ in NGC 3627 (Fig. 8). In a few cases we get nonphysical values for the cross-correlation peaks; this occurs when we correlate either noise features or weak emission that is well outside the bar. The arrows point toward the nonphysical value of the cross-correlation peak, off the scale shown in these figures.

Though there appears to be a relationship between the bar strength and the CO- $\text{H}\alpha$ offset, there is no *systematic* pattern in the offset as a function of the galactocentric

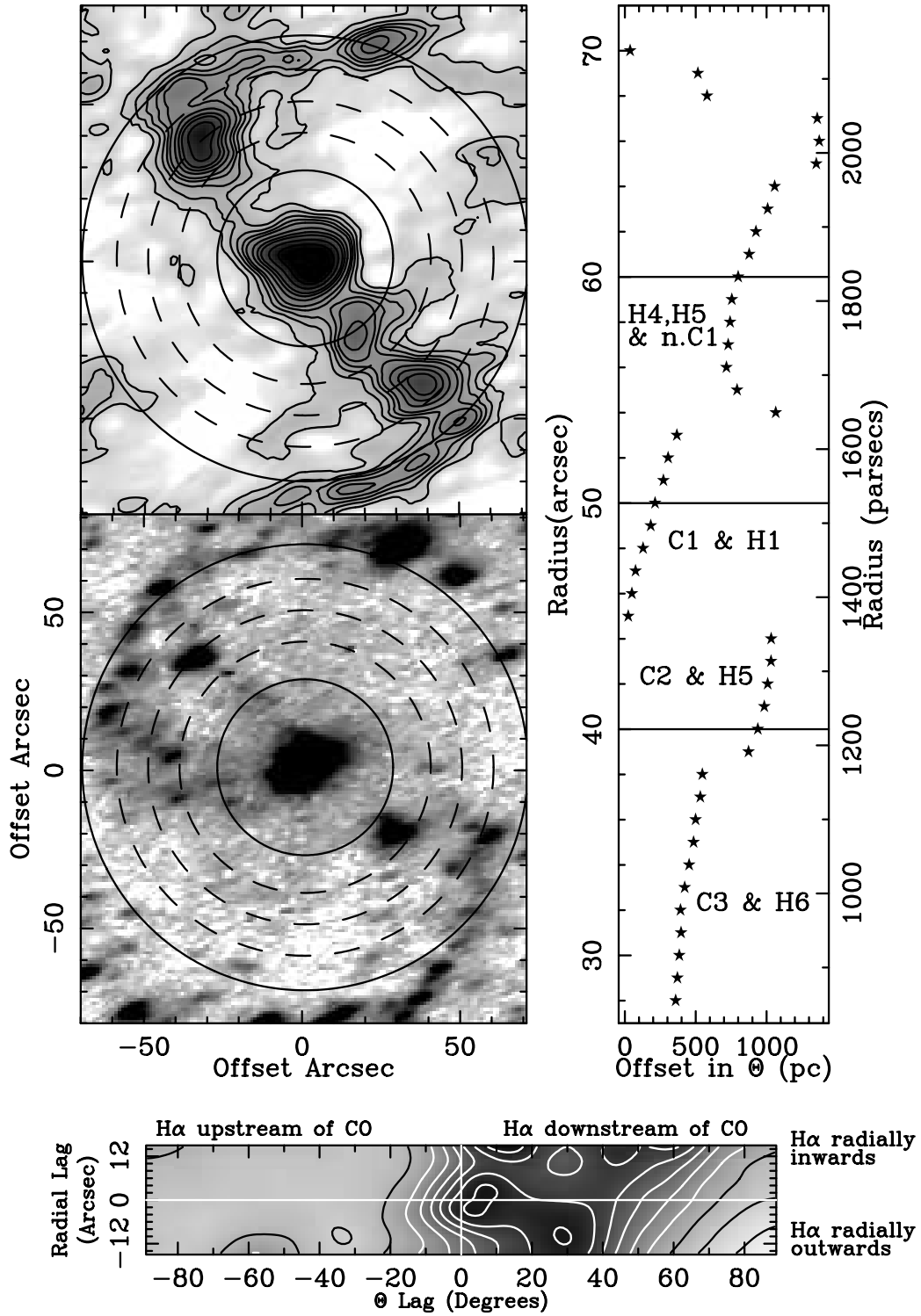


FIG. 7.—NGC 2903: the left column shows the deprojected CO (*top*) and H α (*bottom*) images. The solid circles indicate the boundaries over which the cross-correlation was done. The dashed circles are spaced at 40'', 50'', and 60'' from the nucleus. The vertical panel on the right-hand side shows the maximum of the azimuthal cross-correlation for 1'' radial bins. The annotations refer to the CO or H II regions labeled in Fig. 1. The bottom panel shows the two dimensional cross-correlation values. The contours, drawn at arbitrary levels, highlight peaks and valleys. Notice that the cross-correlation values are highest for H α offset azimuthally downstream (leading side) and radially outward from the CO.

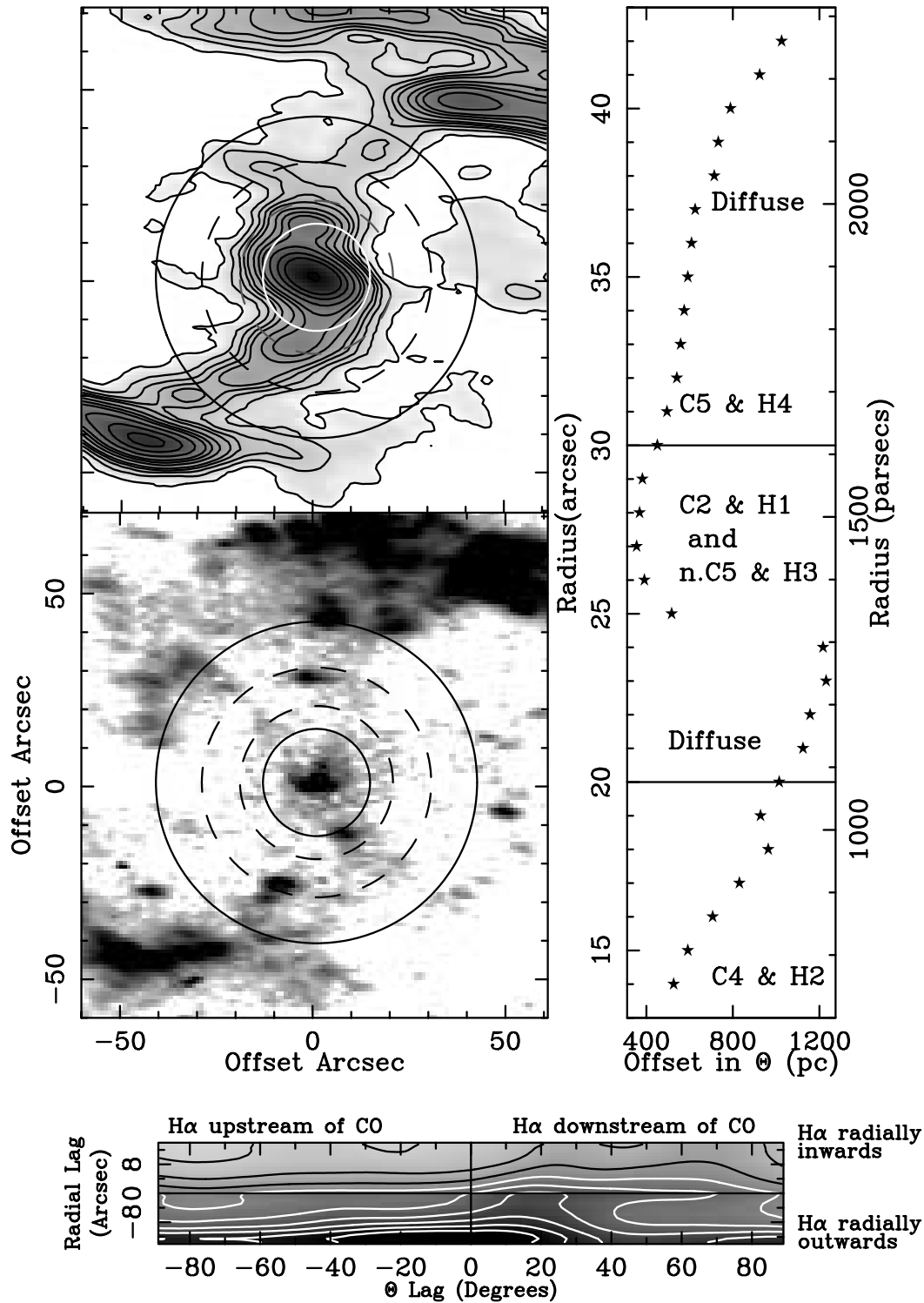


FIG. 8.—NGC 3627: same as Fig. 7. Diffuse indicates correlation between diffuse H α and CO. The notation “n.C5” refers to the northern side of the region C5.

radius. We often see a trend of increasing offsets of H α from CO over radial extents of 5''–10'', e.g., the radial bins between 38''–42'' (C2 and H5) in Figure 7. This trend is due to beam smearing and subsequent deprojection of the images. These results are discussed further in § 4.

3.2.3. Results of the Two-dimensional Cross-Correlation

The two-dimensional correlation results are plotted in the bottom panels in Figures 7–12. In these panels the intersecting straight lines indicate the 0, 0 lag position. Positive (neg-

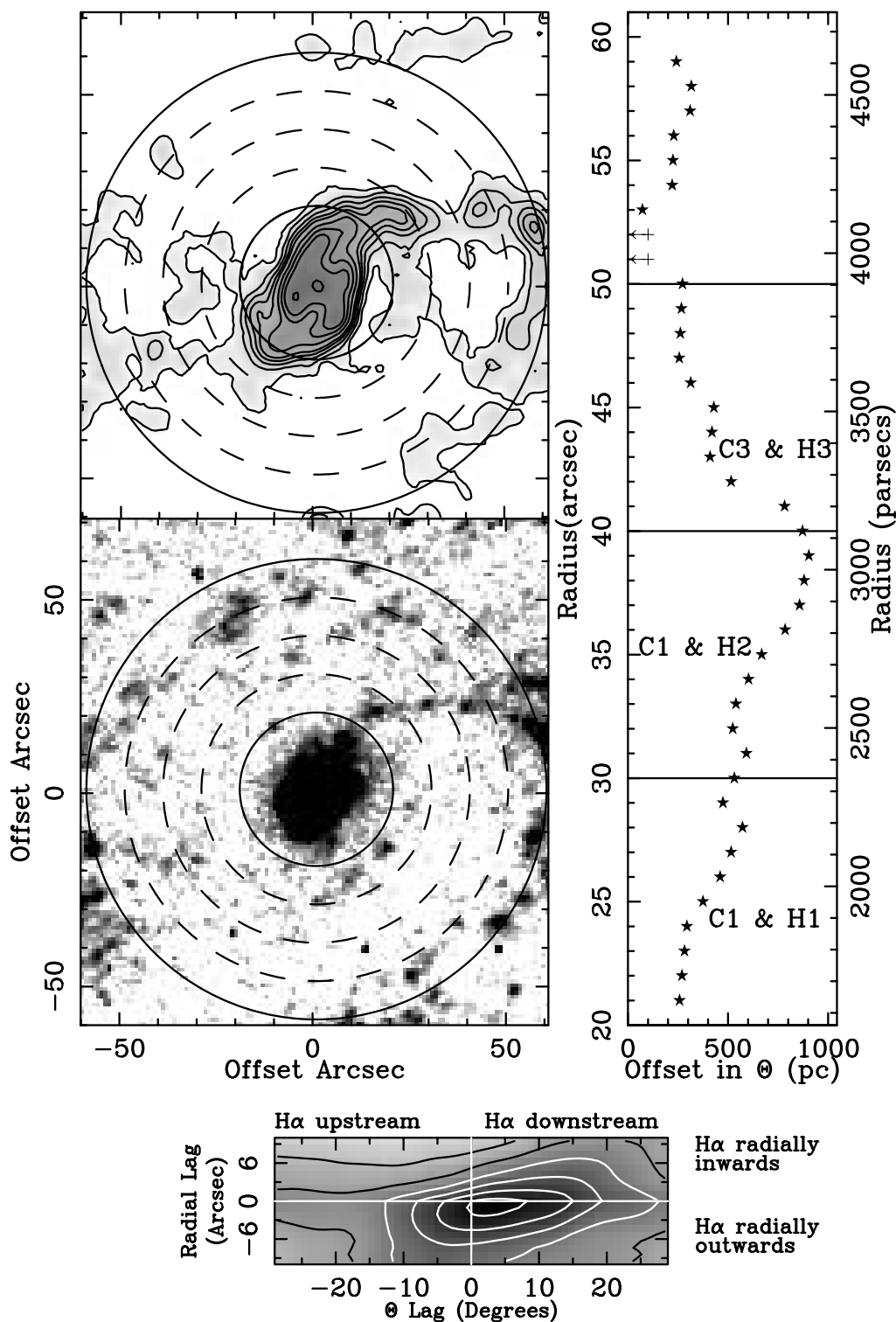


FIG. 9.—NGC 4321: same as Fig. 7. The arrows at 51 and 52'' indicate nonphysical lags, where the maximum of the cross-correlation is dominated by a correlation between diffuse and unrelated CO and H α emission in the annuli.

ative) correlation values indicate H α offset radially inward (outward) or azimuthally leading (trailing) the CO. Unlike in the one-dimensional analyses, where we only correlated 1'' annuli, the location of the cross-correlation maximum (or maxima) in the two-dimensional analyses is susceptible to bright emission near the circumnuclear or bar-end

regions because we sum over the whole bar region. While we did our best to choose an inner boundary to avoid most of the circumnuclear emission, the outer boundary sometimes included bar-end/spiral arm emission (for instance, in NGC 2903). This is one of the reasons why the two dimensional cross-correlation results are less reliable than the other

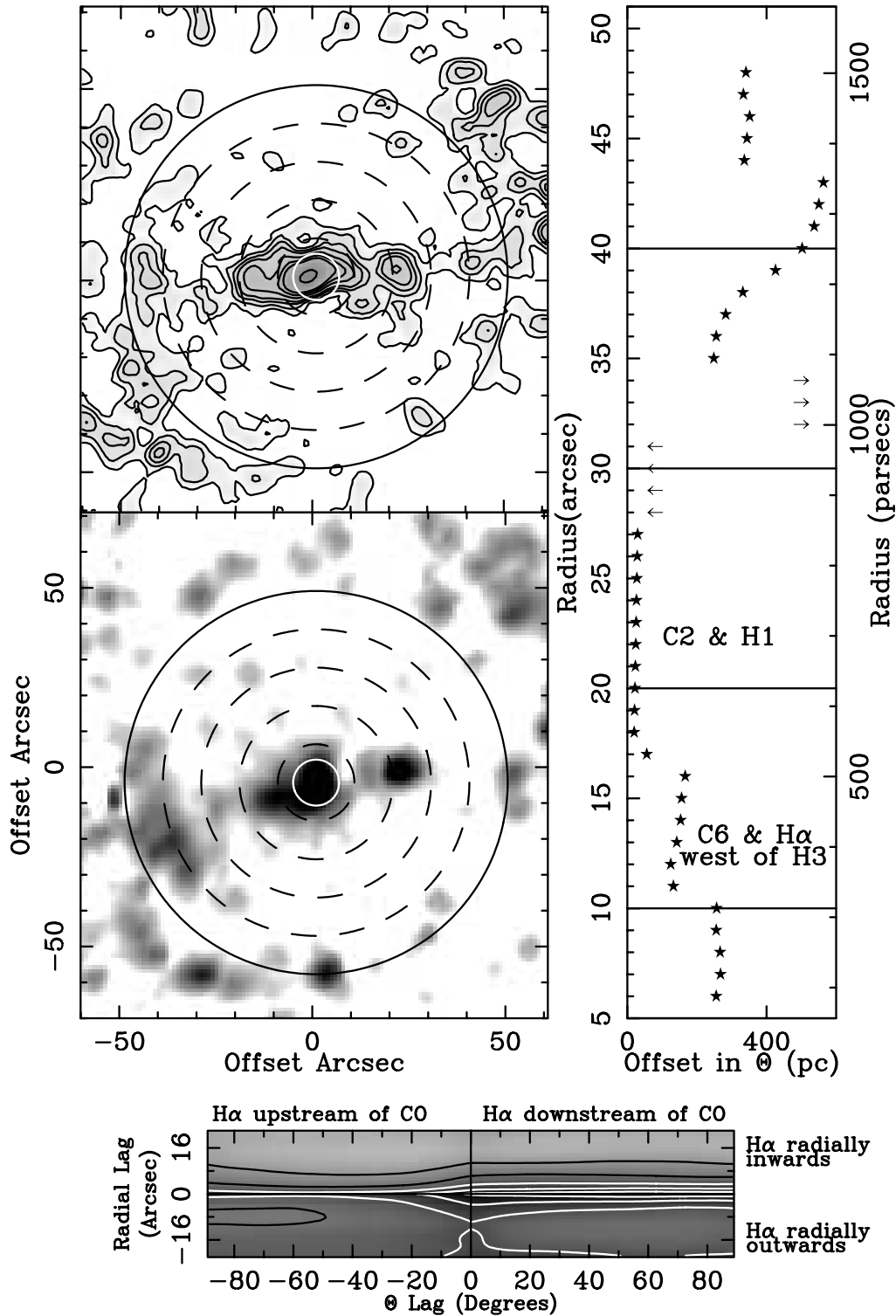


FIG. 10.—NGC 5457: same as previous figures

analyses presented here. Another is the possibility of getting incorrect results because we may correlate physically unrelated peaks. Suppose the brightest H II region is at the outer bar end, whereas the brightest CO peak is at the inner bar end. Then the cross-correlation peak will be at the radial lag at which these peaks overlap. But these regions are most likely unrelated. Though we restricted the radial lag space to

avoid such extreme situations, one must treat the two dimensional cross-correlation results with caution.

In all six galaxies the H α is leading the CO emission in the azimuthal direction. In other words, the correlation values are higher on the right-hand side of the bottom panel. This is consistent with the overlays (§ 3.1) and the one-dimensional cross-correlation analyses (§ 3.2.1). We

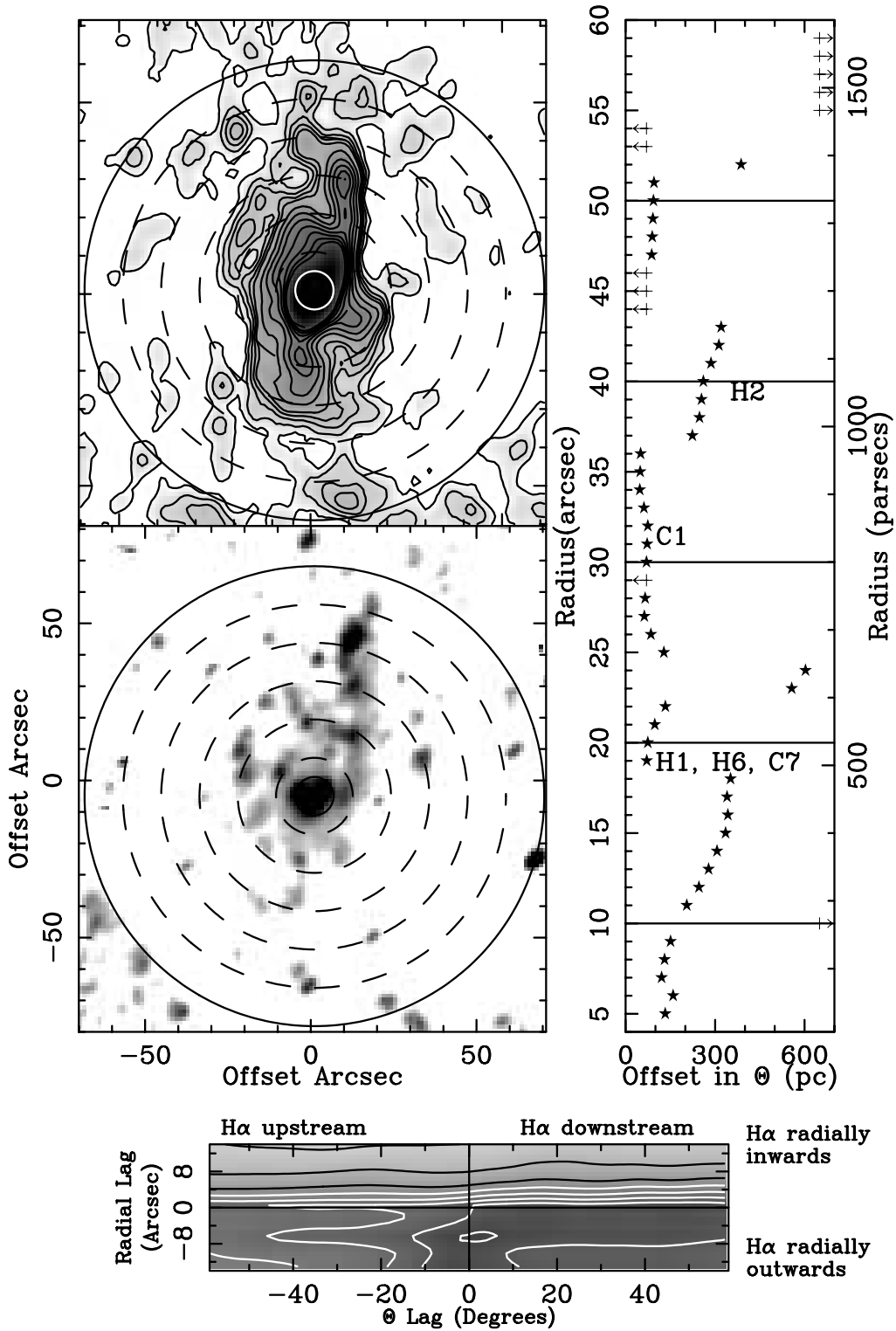


FIG. 11.—NGC 6946: same as previous figures

also find that, in almost all cases, there are higher cross-correlation values for H α offset radially outward from the CO. In four galaxies (NGC 2903, 3627, 6946, and IC 342), the maximum of the cross-correlation values is located at outward radial lags of $\sim 7''$ – $10''$. These large offsets are not obvious in the overlays of CO and H α images and may not be physically meaningful because, as

discussed above, the correlation is between H α and CO peaks along the dust lane.

4. DISCUSSION

How can one explain the CO-H α offset? If there were no relative motion of the gas and stars, then the CO and

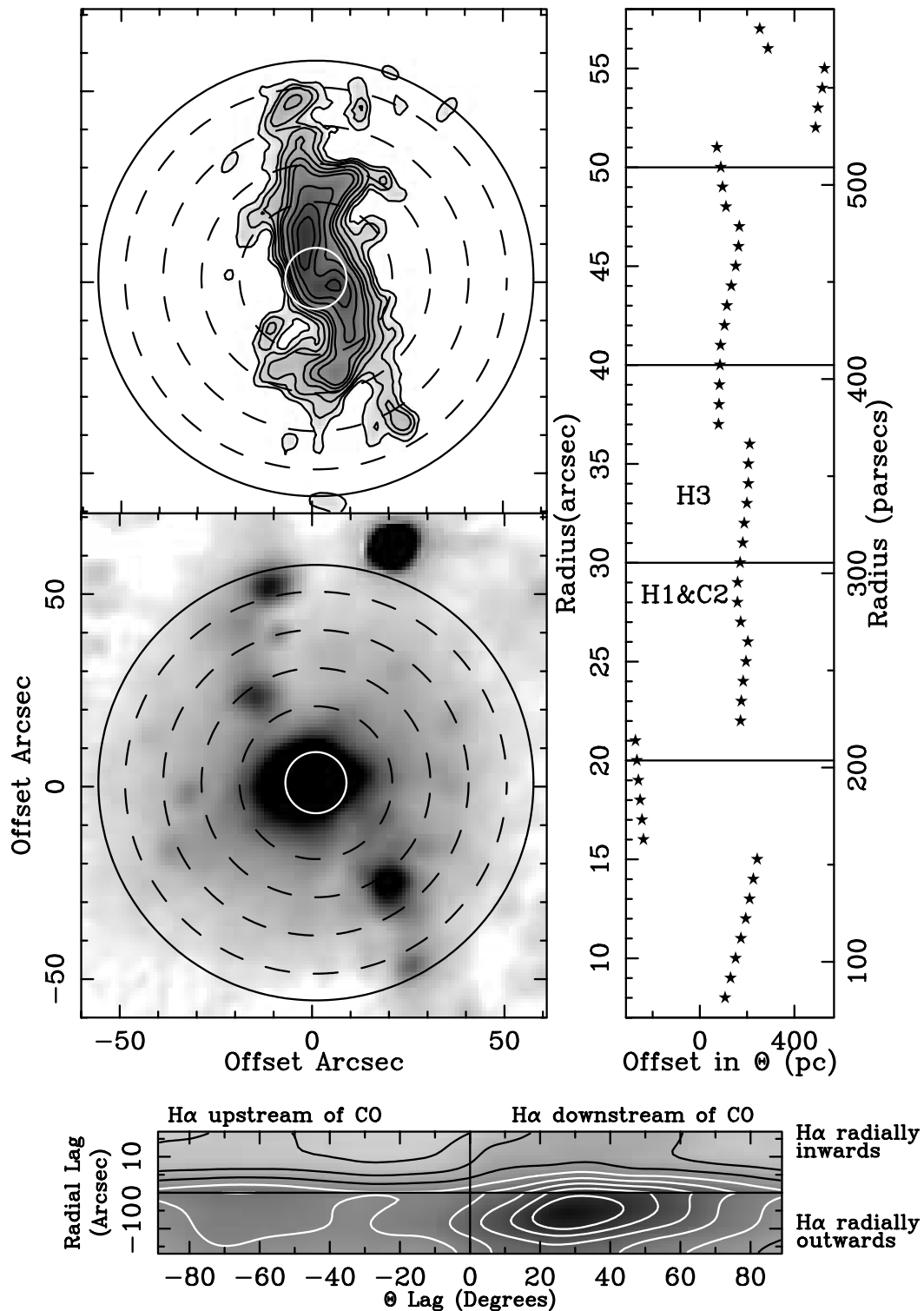


FIG. 12.—IC 342: same as previous figures

H α should be cospatial. However, since the majority of the H α emission is preferentially on the leading side of CO in all six bars, gas dynamics must play a role. Hence, we consider the two main classes of bar gas-flow models: (1) *N*-body/sticky particle models, which treat the gas as

a collection of sticky particles reacting to a gravitational field and exchanging angular momentum and energy upon collisions (e.g., Combes & Gerin 1985), and (2) grid-based hydrodynamic models, which treat the gas as an isothermal, ideal fluid obeying standard hydrodynamic

equations (e.g., Athanassoula 1992a, 1992b; Piner et al. 1995). We use the framework provided by these models to understand the observed CO-H α offsets.

4.1. *An Important Caveat: Detection Limits on the Molecular Gas Data*

The addition of single-dish (NRAO 12 m) on-the-fly data to the BIMA interferometric observations greatly reduced the problem of spatial filtering. As discussed by Helfer et al. (2002a, 2002b), the combined data, such as those presented here, recovers 80%–90% of the flux density for all sources of size less than 10'', with the recovery improving for smaller scales. At the mean distance to these six galaxies (8.25 Mpc), 10'' subtends a linear scale of 400 pc, much larger than a typical giant molecular cloud (~ 40 –50 pc, Scoville 1990) and larger than most giant molecular complexes or associations (~ 100 –400 pc, Rand 1993). So these data do not suffer greatly from the spatial filtering of an interferometer.

The sensitivity of these observations is discussed in detail in Helfer et al. (2002b). We summarize the main points here. Given our typical rms noise of 58 mJy beam $^{-1}$, we have a rms column density sensitivity of 4.6 M_{\odot} pc $^{-2}$, using a CO/H $_2$ conversion factor of 2×10^{20} cm $^{-2}$ (K km s $^{-1}$) $^{-1}$ in a 10 km s $^{-1}$ channel. The data quality is such that the edges of extended emission are probably reliable at 2 σ or 9.1 M_{\odot} pc $^{-2}$, and isolated points are reliable at 3 σ or 13.7 M_{\odot} pc $^{-2}$. For comparison, the mean surface density of a Galactic giant molecular cloud in the solar neighborhood is 50–100 M_{\odot} pc $^{-2}$ (Blitz 1993) within an area of 2.1×10^3 pc 2 . Assuming that this surface density is typical for molecular gas, we are sensitive to clouds with typical masses $\sim 10^6 M_{\odot}$ in a single beam, or, in other words, we would detect large molecular clouds in a single beam, but our observations would not detect a $10^5 M_{\odot}$ cloud. Hence it is possible that we are not detecting molecular gas from small, weak clouds that may be associated with the observed H II regions. This caveat applies throughout our discussion.

Our analysis is focussed on the observed offset between the CO and H α emission. The basic assumption is that these observations trace the highest surface density CO emission, i.e., the regions most prone to star formation activity. In the next two sections we discuss how star formation may occur given the gas flow in the *N*-body/sticky particle and hydrodynamic models.

4.2. *Gas Flow and Star Formation in the N-Body/Sticky Particle Models*

The *N*-body/sticky particle simulations (e.g., Combes & Gerin 1985) are designed to emulate the behavior of bound, molecular clouds, the basic organizational unit of the molecular interstellar medium. However, these models parameterize the physics involved by using ad hoc equations for simulating the collisions and energy exchange. Though they have been successful at reproducing curved dust lanes and rings (Combes 1996), they are unable to reproduce the sharp velocity jumps and straight dust lanes observed in strongly barred spirals.

In these models the bar dust lane results from orbit crowding, similar to a spiral arm dust lane (see Fig. 10 in Regan, Sheth, & Vogel 1999). Gas clouds in these models crowd together and probably form giant molecular complexes in the dust lane; they eventually leave the dust lane, diverging outward on the leading side of the bar. If stars

form in the molecular complexes, as suggested for the spiral arm of M51 (Vogel, Kulkarni, & Scoville 1988), then we naturally expect H α emission to be both in the dust lane and downstream from it. Thus these models naturally fit the observed CO-H α offset seen in our sample. They may also explain the presence of H α emission on the trailing side of the dust lane by arguing that, as the clouds gradually converge on the trailing side, they may collide, form complexes, and form stars. Also, as noted by (Vogel, Kulkarni, & Scoville 1988), the molecular gas clouds are difficult to detect on the leading (downstream) side of the dust lane because the average gas surface density decreases as the clouds diverge outward from the dust lane. These models cannot easily explain the radially outward H α offset seen in the two-dimensional cross-correlation diagrams because, over most of the bar, the cloud orbits have a radially inward component as clouds converge toward the dust lane.

4.3. *Gas Flow and Star Formation in Hydrodynamic Models*

In contrast to the *N*-body/sticky particle models, hydrodynamic simulations use standard fluid equations to model the gas, but the gas is usually an isothermal, ideal fluid. Though self-gravity and magnetic fields have not been included in the past, newer models have begun to incorporate these as well (e.g., Kim & Ostriker 2002). In contrast to the *N*-body/sticky particle models, the hydrodynamic models have been successful, not only at reproducing the observed gas kinematics (Regan, Vogel, & Teuben 1997; Regan et al. 1999), but also the entire range of observed bar dust lane shapes, from curved to straight (Athanassoula 1992b).

The gas kinematics in these models are dramatically different (see Fig. 9 in Regan et al. 1999). The gas streamlines diverge as they approach the dust lane (Regan et al. 1997). At the dust lane *all* of the gas is redirected inward by a hydrodynamic shock such that *none* of the gas crosses the dust lane. Historically, the bar dust lanes, despite their high gas density, are regarded as inhospitable environments for star formation because of high shear (Athanassoula 1992b and references therein). Regan et al. (1997) have also argued that the diverging streamlines on the trailing side of the dust lane can tear apart molecular clouds or at least prevent molecular complexes from forming (but note that self-gravity can counteract this effect; see discussion in Sheth et al. 2000). These studies argue effectively for reduced star formation efficiency in the dust lanes.

Even if stars form in the dust lane, the gas flow dictates that stellar clusters travel down the dust lane. Thus these models cannot naturally explain the azimuthal offset between the H α and the CO. In this model gas flow, the only way for the H II regions to appear on the leading side of the dust lanes is to form stars on the trailing side while the gas still has tangential motion.

Such a mechanism was proposed in a previous study of the barred spiral NGC 5383. In that bar, Sheth et al. (2000) noted that the limited number of H II regions, all on the leading side of the dust lane, were directly across from faint dust spurs. They proposed that, in this bar, stars were forming in spurs because spurs were regions of high gas density and low shear. Spurs are faint and difficult features to detect. Though we see some spurlike CO features, the correlation between H II regions and spurs requires more sensitive CO observations. A more practical approach

would be to first trace the spurs with high-quality (resolution and sensitivity) optical-infrared color maps to understand their locations, structure, and frequency. Then a targeted study with sensitive CO observations can help us better understand the relationship between spurs, CO, and $H\alpha$. Though possible, we feel that it is unlikely that all star formation in bars occurs in spurs. However, we note that, if stars form in the spurs, then the radially outward offset can be naturally explained because the gas streamlines diverge outward on the trailing side of the dust lanes in this model.

In summary, both gas-flow models can explain the CO- $H\alpha$ offsets, but neither is satisfactory, especially when we consider these and previous observations of bars. One possible improvement, especially to the hydrodynamic models, could be the use of a multiphased molecular medium consisting of a diffuse, gravitationally unbound phase (e.g., Elmegreen 1993; Rand et al. 1999; Hüttemeister et al. 2000) and the usual dense, bound phase made of giant molecular clouds (e.g., Scoville 1990; Young & Scoville 1991). In a bar diffuse gas may be formed by the disruption of clouds by the tidal field of a bar or by off-center cloud-cloud collisions (Hüttemeister et al. 2000). At least in one bar, NGC 7479, tentative evidence of diffuse gas has been presented (Hüttemeister et al. 2000). The diffuse gas has a higher velocity width than the bound phase, and so it may dominate the CO kinematics. Perhaps this is why studies of gas kinematics in the dust lane have been consistent with the hydrodynamic models (e.g., Regan et al. 1997; Regan et al. 1999). And it may be that the star-forming component of the gas, the dense, bound clouds, behaves more like the sticky particles in N -body simulations.

4.4. Timescales and Cloud Speeds in Context of Model Gas Flows

Previous spiral arm studies found $H\alpha$ offset from the CO by a few hundred parsecs (Vogel, Kulkarni, & Scoville 1988; Rand 1993; Knapen & Beckman 1996; Loinard et al. 1996). Vogel et al. (1988) immediately recognized that this offset was too large, given that typical “drift” velocity of a cloud across a spiral arm is $\sim 10 \text{ km s}^{-1}$. They suggested that stars may be forming after a “gestation” period of a few million years following the compression of clouds by the spiral density wave.

The situation is different in the bar environment. In the N -body/sticky particle model for bars, the orbit crowding is much more severe than for a spiral arm shock, and it is non-trivial to calculate an equivalent “drift” velocity across the bar dust lane. The offsets observed along most of the bar dust lanes (0–500 pc, § 3.2.2) are similar to those observed along spiral arms. Therefore, if the drift velocity in bars is similar to that in spiral arms, similar “gestation” periods are necessary in the framework of the N -body/sticky particle gas-flow model. However, in one or two locations along bars in NGC 2903 and NGC 3627 we measure offsets as large as $\sim 800 \text{ pc}$. Then, for the star formation scenario presented here in the framework of N -body/sticky particle gas-flow model, either unusually large gestation periods and/or large drift velocities are required. One observational test may be to measure speeds of newly formed clusters, using stellar absorption lines to better understand the dynamics. Another possibility is that for these particular cases, our basic assumption that these stars formed in the dust lanes is not applicable (see the caveat in § 4.1).

In the framework of the hydrodynamical models there is no “drift” velocity because all of the gas is redirected inward by the shock. Suppose the newly formed stars inherit the speed of their parent molecular clouds. Then, to traverse the *entire* range of offsets seen in these bars (0–800 pc, § 3.2.2), the velocity for a stellar cluster must be 0–80 km s^{-1} , assuming a timescale of 10 Myr for the $H\alpha$ peaks. Individual H II regions have lifetimes $\sim 3 \text{ Myr}$ (Spitzer 1978), but, since we do not resolve individual H II regions at these distances, we assume a larger lifetime for the $H\alpha$ peaks because they are most likely a collection of H II regions.

The relative speed of clouds entering the bar pattern is high. Though difficult to quantify, a few direct measurements of bar pattern speeds indicate values between 50–65 $\text{km s}^{-1} \text{ kpc}^{-1}$ (Merrifield & Kuijken 1995; Dehnen 1999; Gerssen, Kuijken, & Merrifield 1999). Hydrodynamic models that try to reproduce observations use a bar pattern speed of 30–35 $\text{km s}^{-1} \text{ kpc}^{-1}$ (Piner et al. 1995), but these bars are longer than typically observed. In any case, both the models and observations indicate that bars end at $\sim 80\%$ of their corotation radius, consistent with the findings of Athanassoula (1992a, 1992b).

Using this empirical relationship and deprojected bar lengths (Table 5 from Sheth et al. 2002), the bar pattern speeds in five of six galaxies were measured using CO rotation curves by Das et al. (2001) to be: 68 $\text{km s}^{-1} \text{ kpc}^{-1}$ (NGC 2903), 55 $\text{km s}^{-1} \text{ kpc}^{-1}$ (NGC 3627), 35 $\text{km s}^{-1} \text{ kpc}^{-1}$ (NGC 4321), 71 $\text{km s}^{-1} \text{ kpc}^{-1}$ (NGC 5457), and 55 $\text{km s}^{-1} \text{ kpc}^{-1}$ (NGC 6946). These values are consistent with the direct measurements of bar pattern speeds in other galaxies. The pattern speed of the bar in IC 342 is difficult to estimate because the bar parameters are not well known. We estimated a bar length of $\sim 58''$ (0.6 kpc). For this bar length the pattern speed from the CO rotation curve is 196 $\text{km s}^{-1} \text{ kpc}^{-1}$, an unrealistically high value. If instead we use a length of $4''$, as suggested by Crosthwaite et al. (2001), and assume that the rotation curve remains flat at $\sim 141 \text{ km s}^{-1}$, then the bar pattern speed would be a more reasonable 81 $\text{km s}^{-1} \text{ kpc}^{-1}$. We do not use IC 342 in the ensuing discussion.

The speed at which a molecular cloud enters is the difference between the disk and bar pattern speeds. Hence, at the midpoints of these bars, cloud speed varies from 49–99 km s^{-1} . So, in the context of the hydrodynamical models, if a stellar cluster forms from clouds upstream of the shock, it would inherit a velocity of this magnitude. The velocity of the clouds upstream of the shock is primarily tangential to the bar dust lane. Hence, while the gas is redirected inward down the dust lane, newly formed stellar clusters continue on the original orbits, and the observed range of offsets is consistent with the expected cloud speeds. However, we emphasize that the range of CO- $H\alpha$ offsets in a bar is not correlated with the galactocentric radius. This suggests that star formation is not a simple function of the parent cloud speed, or alternatively a function of the shock strength. Consistent with this conclusion is the range in offsets observed in a single bar, which suggests that star formation depends on other factors, e.g., gas surface density, and/or local shear.

5. CONCLUSIONS

We have investigated the distribution of molecular gas and star-forming regions in the bars of six spirals from the

BIMA Survey of Nearby Galaxies. Our main conclusions are as follows:

1. The CO emission is brightest along the leading edges of the bar. Weak spurs of CO emission are seen on the trailing side of the dust lanes. These spurs may play a role in star formation upstream of the dust lane. At the bar ends strong CO and H α emission are seen on the trailing and leading sides; these may be the beginnings of inner rings.

2. The H α emission is distributed in compact and diffuse structures. There are a few instances where the H α is coincident with or on the trailing side of the CO emission. But the main result is that, in all six cases, the majority of the H α emission is offset toward the leading side of the CO.

3. We quantify the offsets using a cross-correlation analysis and find a range of 0–800 pc, with larger offsets in stronger bars. However, in a given bar there is a range of offsets, and there is no systematic pattern as a function of the galactocentric radius.

4. In the two-dimensional cross-correlation analysis there is a tendency for the H α emission to be offset radially outward from the CO emission. However, this trend is less significant than the azimuthal offsets because correlations in two dimensions can be between physically unrelated H II and CO regions.

5. The observed CO-H α distributions may be explained by either the *N*-body/sticky particle models or

the hydrodynamic models, with different, plausible star formation scenarios. In the context of the *N*-body simulations stars may form via cloud-cloud agglomeration in the dust lanes. In the context of the hydrodynamic models the stars could form in dust spurs on the trailing side of the dust lane. We suggest that the addition of a two-phased or multiphased molecular medium can improve the agreement between these and previous observations, and gas-flow models in bars.

This work would not have been possible without the rest of the SONG team members (T. Wong, T. Helfer, L. Blitz, and D. Bock) and the dedicated observatory staff at Hat Creek and at the Laboratory for Millimeter-Wave Astronomy at the University of Maryland. We thank S. Aalto, S. Hüttemeister, J. Kenney, E. Ostriker, N. Scoville, E. Schinnerer, J. Stone, and T. Treu for invaluable and insightful discussions about gas kinematics and star formation. We are grateful to N. Reddy and E. Schinnerer for their careful reading and helpful comments, which significantly improved this paper. Research with the BIMA array is supported by NSF grant AST 99-81289. Support for the Laboratory for Millimeter-Wave Astronomy is also provided by the state of Maryland. This research is also partially funded by NSF grant AST 99-81546.

REFERENCES

- Athanassoula, E. 1992a, MNRAS, 259, 328
 ———. 1992b, MNRAS, 259, 345
 Benedict, F. G., Smith, B. J., & Kenney, J. D. P. 1996, AJ, 111, 1861
 Blitz, L. 1993, Protostars and Planets III, ed. E. H. Levy & J. I. Lunine (Tucson: Univ. Arizona Press), 12
 Buta, R., & Block, D. L. 2001, ApJ, 550, 243
 Buta, R., & Combes, F. 1996, Fundam. Cosmic Phys., 17, 95
 Buta, R., Treuthardt, P. M., Byrd, G. G., & Crocker, D. A. 2000, AJ, 120, 1289
 Combes, F. 1996, in IAU Colloq. 157, Barred Galaxies, ed. R. Buta, D. A. Crocker, & B. G. Elmegreen (San Francisco: ASP), 286
 Combes, F., & Gerin, M. 1985, A&A, 150, 327
 Crosthwaite, L. P., Turner, J. L., Hurt, R. L., Levine, D. A., Martin, R. N., & Ho, P. T. P. 2001, AJ, 122, 797
 Das, M., Teuben, P. J., Vogel, S. N., Harris, A., Regan, M. W., Sheth, K., Helfer, T. T., & Thornley, M. D. 2001, BAAS, 199, No. 58.12
 Dehnen, W. 1999, ApJ, 524, 35
 Downes, D., Reynaud, D., Solomon, P. M., & Radford, S. J. E. 1996, ApJ, 461, 186
 Eckart, A., Cameron, M., Jackson, J. M., Genzel, R., Harris, A. I., Wild, W., & Zinnecker, H. 1991, ApJ, 372, 67
 Elmegreen, B. G. 1993, ApJ, 411, 170
 Elmegreen, B. G., & Elmegreen, D. M. 1985, ApJ, 288, 438
 Eskridge, P., et al. 2000, AJ, 119, 536
 Ferrarese, L. et al. 1996, ApJ, 468, L95
 Gerksen, J., Kuijken, K., & Merrifield, M. R. 1999, MNRAS, 306, 926
 Gruendl, R. 1996, Ph.D. thesis, Univ. Maryland
 Handa, T., Nakai, N., Sofue, Y., Hayashi, M., & Fujimoto, M. 1990, PASJ, 42, 1
 Helfer, T. T., Thornley, M. D., Regan, M. W., Wong, T., Sheth, K., Vogel, S. N., Blitz, L., & Bock, D. C.-J. 2002, ApJS, submitted
 Helfer, T. T., Vogel, S. N., Lugten, J. B., & Teuben, P. J. 2002, PASP, 114, 350
 Hüttemeister, S., Aalto, S., Das, M., & Wall, W. F. 2000, A&A, 363, 93
 Karachentsev, I. D., & Tikhonov, N. A. 1993, A&AS, 100, 227
 Kenney, J. D. P., Carlstrom, J. E., & Young, J. S. 1993, ApJ, 418, 687
 Kenney, J. D. P., Scoville, N. Z., & Wilson, C. D. 1991, ApJ, 366, 432
 Kim, W. T., & Ostriker, E. C., 2002, ApJ, 570, 132
 Knäpen, J. H., & Beckman, J. E., 1996, MNRAS, 283, 251
 Loinard, L., Dame, T. M., Koper, E., Lequeux, J., Thaddeus, P., & Young, J. S. 1996, ApJ, 469, L101
 Lord, S. D., & Kenney, J. D. P. 1991, ApJ, 381, 130
 Martin, P., & Friedli, D. 1997, A&A, 326, 449
 Merrifield, M. R., & Kuijken, K. 1995, MNRAS, 274, 933
 Miyashiro, G. M. 1982, ZODIAC User's Manual
 Ohta, K., Sasaki, M., & Saito, M. 1986, PASJ, 38, 677
 Ondrechen, M. P. 1985, AJ, 90, 1474
 Phillips, A. C. 1996, in IAU Colloq. 157, Barred Galaxies, ed. R. Buta, D. A. Crocker, & B. G. Elmegreen (San Francisco: ASP), 44
 Piner, B. G., Stone, J. M., & Teuben, P. J. 1995, ApJ, 449, 508
 Planesas, P., Colina, L., & Perez-Olea, D. 1997, A&A, 325, 81
 Rand, R. J. 1993, ApJ, 404, 593
 Rand, R. J., Lord, S. D., & Higdon, J. L. 1999, ApJ, 513, 720
 Regan, M. W., & Elmegreen, D. M. 1997, AJ, 114, 965
 Regan, M. W., Helfer, T. T., Thornley, M. D., Sheth, K., Wong, T., Vogel, S. N., Blitz, L., & Bock, D. C.-J. 2001, ApJ, 561, 218
 Regan, M. W., Sheth, K., & Vogel, S. N. 1999, ApJ, 526, 97
 Regan, M. W., Sheth, K., Vogel, S. N., & Teuben, P. J. 2002, ApJ, 574, 126
 Regan, M. W., & Vogel, S. N. 1995, ApJ, 452, L21
 Regan, M. W., Vogel, S. N., & Teuben, P. J. 1997, ApJ, 482, L143
 Roberts, W. W., Jr., Huntley, J. M., & van Albada, G. D. 1979, ApJ, 233, 67
 Roy, J., & Belley, J. 1993, ApJ, 406, 60
 Saha, A., Sandage, A., Tammann, G. A., Labhardt, L., Macchetto, F. D., & Panagia, N. 1999, ApJ, 522, 802
 Sakamoto, K., Okumura, S., Minezaki, T., Kobayashi, Y., & Wada, K. 1995, AJ, 110, 2075
 Sault, R. J., Teuben, P. J., & Wright, M. C. H. 1995, in ASP Conf. Ser. 77, Astronomical Data Analysis Software and Systems IV, ed. R. A. Shaw, H. E. Payne, & J. J. E. Hayes (San Francisco: ASP), 433
 Sempere, M. J., & Garcia-Burillo, S. 1997, A&A, 325, 769
 Scoville, N. Z. 1990, in ASP Conf. Proc. 12, The Evolution of the Interstellar Medium (San Francisco: ASP), 49
 Sellwood, J. A., & Wilkinson, A. 1993, Rep. Prog. Phys., 56, 173
 Sharina, M. E., Karachentsev, I. D., & Tikhonov, N. A. 1997, Astron. Lett., 23, 373
 Sheth, K. 2001, Ph.D. thesis, Univ. Maryland
 Sheth, K., et al. 1998, BAAS, 193, No. 70.12
 Sheth, K., Regan, M. W., Vogel, S. N., & Teuben, P. J. 2000, ApJ, 532, 221
 Sheth, K., et al. 2002, ApJ, submitted
 Shopbell, P. L. 1998, ZODIAC+ User's Manual, 2d ed.
 Spitzer, L., Jr. 1978, in Physical Processes in the Interstellar Medium (New York: Wiley)
 Stetson, P. B. et al. 1998, ApJ, 508, 491
 Vogel, S. N., Kulkarni, S. R., & Scoville, N. Z. 1988, Nature, 334, 402
 Vogel, S. N., Weymann, R., Rauch, M., & Hamilton, T. 1995, ApJ, 441, 162
 Young, J. S., & Scoville, N. Z. 1991, ARA&A, 29, 581